ELSEVIER

Contents lists available at ScienceDirect

# Computers and Fluids

journal homepage: www.elsevier.com/locate/compfluid





# Effectiveness of RANS in predicting indoor airborne viral transmission: A critical evaluation against LES

K. Choudhary <sup>a</sup>, K.A. Krishnaprasad <sup>b</sup>, S. Pandey <sup>c</sup>, N. Zgheib <sup>d,\*</sup>, J.S. Salinas <sup>b</sup>, M.Y. Ha <sup>a</sup>, S. Balachandar <sup>b</sup>

- a School of Mechanical Engineering, Pusan National University, Busan, Republic of Korea
- b Department of Mechanical and Aerospace Engineering, University of Florida, Gainesville, FL 32611, USA
- <sup>c</sup> Rolls-Royce and Pusan National University Technology Centre in Thermal Management, Busan, Republic of Korea
- d Department of Mechanical Engineering, The University of Texas Rio Grande Valley, Edinburg, TX 78573, USA

#### ARTICLE INFO

#### Keywords: Indoor airborne transmission RANS simulation Correction to well-mixed model Covid-19 Large eddy simulation (LES) Indoor air quality

#### ABSTRACT

We investigate the dispersal of droplet nuclei inside a canonical room of size  $10 \times 10 \times 3.2 \, \text{m}^3$  with a four-way cassette air-conditioning unit placed at the center of the ceiling. We use Reynolds averaged Navier–Stokes (RANS) simulations with three flow rates corresponding to air changes per hour (ACH) values of 2.5, 5, and 10. The room setup as well as the operating conditions are chosen to match those of a recent high-fidelity large eddy simulation (LES) study. We use statistical overloading with a total of one million droplet nuclei being initially distributed randomly with uniform probability within the room. Six nuclei sizes are considered ranging in radius from 0.1 to  $10 \, \mu m$  (166,667 nuclei per size). The simulations are one-way coupled and employ the Langevin equations to model sub-grid motion. The flow and particle statistics are compared against the reference LES simulations, and we find that the RANS  $k-\varepsilon$  realizable model may be used as a computationally cheaper alternative to LES for predicting pathogen concentration in confined spaces albeit, with potentially increased statistical discrepancy.

### 1. Introduction

The Covid-19 pandemic has emphasized the need for accurate risk assessment in indoor settings where the risk of infection or transmissibility is relatively high. Accurate risk assessments would inform policy makers and help them propose the necessary mandates to protect the community with the least adverse impact on society. This necessitates a better understanding of the characteristics of the virus, the risk tolerance and susceptibility of the indoor occupants, as well as how the airborne virus-laden droplet nuclei are distributed within the room in question. The latter of the three components is inherently a fluid mechanics problem that involves tracking droplet nuclei ejected from a host during an expiratory activity such as breathing, talking, singing, coughing, etc.

From a fluid mechanics perspective, indoor airborne transmission is usually studied at either the ejection scale [1–4] or the room scale [5–9]. The ejection scale problem consists of understanding the spatial extent of the ejected droplet cloud shortly following an expiratory event, and its main focus is establishing the amount and size distribution of virus-laden droplet nuclei that remain airborne. The factors that affect the above outcomes do correspond to both the expiratory event

itself and the ambient temperature and humidity, which control droplet evaporation [10,11]. For the ejection scale problem, the time scale of interest is only on the order of few seconds, since after this early period, the dynamics of the airborne nuclei depend on the ambient flow and not on the initial ejection activity.

On the other hand, the room scale problem focuses on long term dispersal of the airborne virus-laden nuclei within the indoor space [12]. Here, the droplet nuclei are kept airborne for an extended period by turbulence, and the time scale of interest is usually on the order of minutes to hours. It should be pointed out that while the nuclei continually settle down and deposit on the floor, even fairly larger droplet nuclei of diameter 50  $\mu$ m, remain airborne for minutes in a canonical room with typical ventilation conditions [13].

To assess the risk of infection in an indoor setting, the quanta of pathogen being inhaled by a susceptible recipient must be estimated. This in turn requires the evaluation of the concentration of pathogen-containing droplet nuclei within the room. The well-mixed model [12, 14,15] is very effective in estimating the room-averaged concentration under a wide variety of conditions. The well-mixed assumption greatly simplifies the complex space and time-dependent distribution of nuclei

E-mail addresses: nadim.zgheib@utrgv.edu (N. Zgheib), myha@pusan.ac.kr (M.Y. Ha), bala1s@ufl.edu (S. Balachandar).

<sup>\*</sup> Corresponding author.

concentration within an indoor space. This simplification allows the well-mixed model to easily account for virological factors such as infectivity, susceptibility, viral deactivation, and effects such as the use of masks and other types of filtration [16]. Recent room-scale simulations of natural and forced ventilation flows have shown that the room-averaged nuclei concentration is well predicted by the well-mixed model to within a few percent [13].

The limitation of the well-mixed theory is that it assumes the pathogen-laden airborne droplet nuclei released by the infected individual to instantly mix within the indoor space and be readily available to anyone within the room at equal probability. The well-mixed theory neither accounts for the distance between the infected and the susceptible individuals, nor distinguishes between the different levels of turbulent mixing in the inlet jets, corners of the room, etc. As a result, risk assessments based on the well-mixed model can be either overly restrictive or too lax. The LES simulations of Salinas et al. (2022) [13] observed that for separation distances in excess of 5 m between the infected and the susceptible individuals the well-mixed model is generally overly-restrictive in its risk assessment. Whereas, at closer separations the quanta of pathogen inhaled can be substantially larger than what is predicted by the well-mixed model.

Thus, the well-mixed theory and model provide a solid foundation for evaluating average pathogen concentration in any indoor setting. But one must take into account the effect of non-uniform pathogen distribution within the room, and the actual scenario of where the infected and susceptible individuals are likely to be located within the room in making proper risk assessments. To go beyond the well-mixed model one must perform simulations (or experiments) investigating the turbulent mixing of airborne nuclei ejected from the infected individual within the room. This is however a daunting task due to the countless possibilities that may need to be analyzed.

Take for example the scenario of deciding the optimal seating arrangement of a receptionist and a customer in an indoor office space. In this scenario, the receptionist or the customer may be infected and the goal is to minimize the risk of infection for the other customers. Here for a given room specification (room dimensions, ventilation inlet and outlet size and location, filtration efficiency, etc.), simulations must be performed for each possible seating combination of the infected and the susceptible. Furthermore, the simulations must consider a number of other parameters including different ejection possibilities by the infected (i.e., breathing, talking, coughing, or sneezing), ventilation operating conditions in terms of air changes per hour (ACH), as well as different temperature and humidity settings. Thus, there are many variables whose influence must be considered.

Recently, [13] proposed a novel approach that is able to address the influence of many of the above-listed variables with only a single simulation. They employed a statistical overloading technique to produce statistically-relevant data that covers all the countless aforementioned variations. They exploited the fact that the airborne nuclei do not alter the room-scale flow. Therefore, by distributing a very large number of nuclei over the entire room, they were able to obtain statisticallyconverged predictions for (i) all possible locations of the infected, (ii) all possible locations of the susceptible, and (iii) all possible locations for fixed infected-to-susceptible separation distances, i.e. all possible combinations where the infected and the susceptible are 1 m, 2 m, 4 m, or any other distance apart. Furthermore, their simulations showed that the results from different values of ACH collapsed when properly scaled, and thus it is sufficient to study a single representative ACH. They were also able to provide corrections to the well-mixed model of Bazant and Bush [12] that account for the effect of non-uniformity in the pathogen distribution within the room. The corrections were given in terms of the cumulative exposure time (CET) and were put forth for different separation distances, expiratory activities, and ACH values.

There however remains formidable challenges in answering questions such as what is the optimal size/shape of a classroom or operating theater, and where should the air conditioner inlets and outlets be

placed. To explore sensitivity to such variations, one must perform many simulations for the different room geometries and air conditioner locations. LES remains expensive, and therefore may not be the optimal tool for such an exploration. Reynolds-averaged Navier–Stokes (RANS) simulations require less computational resources and could provide a viable alternative to the expensive LES.

The main purpose of this paper is to provide a thorough comparison between LES and RANS simulations. This will be accomplished by comparing the RANS simulation results to the corresponding high-fidelity LES of [13]. In the RANS approach, different Reynolds stress closure models will be tested to account for the unresolved turbulence and a Langevin model will be used to account for the effect of the unresolved turbulence on the dispersion of the particles. Comparisons will be made for the flow and particle statistics to assess the appropriateness of RANS in producing accurate pathogen concentration distributions. In particular, the statistical overloading technique will be employed in the RANS simulations as well. The RANS results will be compared against the corresponding LES results, not only at the level of room average, but also in terms of different statistical averages including for specific distances between the infected and the susceptible individuals. The focus will be on establishing the following questions: (i) How well does the RANS mean flow and the rms turbulence within the room compare with the corresponding LES results? (ii) Is the room-averaged droplet nuclei concentration obtained from RANS in agreement with the wellmixed theory and LES results? (iii) Does the concentration variation within the room and its dependence on nuclei size obtained in the RANS simulations agree with those from LES? (iv) [13] captured the effect of concentration variation within the room in terms of a simple correction function that depends primarily on the separation distance, as such, how accurately can the RANS simulations obtain the correction function?

Thus, the present work will put RANS simulations to a rigorous test in terms of their ability to capture all the relevant physics of indoor turbulent dispersion of airborne droplet nuclei. If the answers to the above questions are satisfactory, then RANS could be used to establish the validity of the well-mixed assumption and departure from wellmixedness in terms of the correction function for varying room shapes, sizes, and air conditioner configurations. This will result in significant computational savings since we observe the RANS approach to be one order of magnitude cheaper than the LES approach. Furthermore, codes that can readily perform RANS simulations are far more widespread than LES. Thus, once accuracy and limitations are established, the RANS approach can be widely deployed by many users to study airborne spreading of viral infection in many other practical scenarios of interest. There are several recent studies in the literature that have adopted the RANS model in similar problems using the Euler Lagrange framework [17-24]. However, to the best knowledge of the authors, this is the first study in which RANS is used with statistical overloading to estimate the temporal and spatial distribution of droplet nuclei in an enclosed space with detailed comparison of the nuclei statistics against companion LES.

# 2. Numerical setup and mathematical model

The geometrical setup of the RANS simulations is identical to that employed in the LES of Salinas et al. (2022) [13]. It consists of a canonical room of size  $10\,\text{m}\times10\,\text{m}\times3.2\,\text{m}$ , in which a 4-way air-conditioning system is installed at the center of the ceiling. The air-conditioning system consists of one square-shaped outlet located at the center and four rectangular-shaped inlets located on the four sides of the central outlet. The outlet has dimensions of  $60\,\text{cm}\times60\,\text{cm}$ , and the surrounding inlets have individual dimensions of  $5.5\,\text{cm}\times44\,\text{cm}$ . The shape of the system and its placement at the center of the ceiling results in an 8-fold symmetry configuration. The symmetry is with respect to the vertical bisector and diagonal planes as can be seen in Fig. 1.

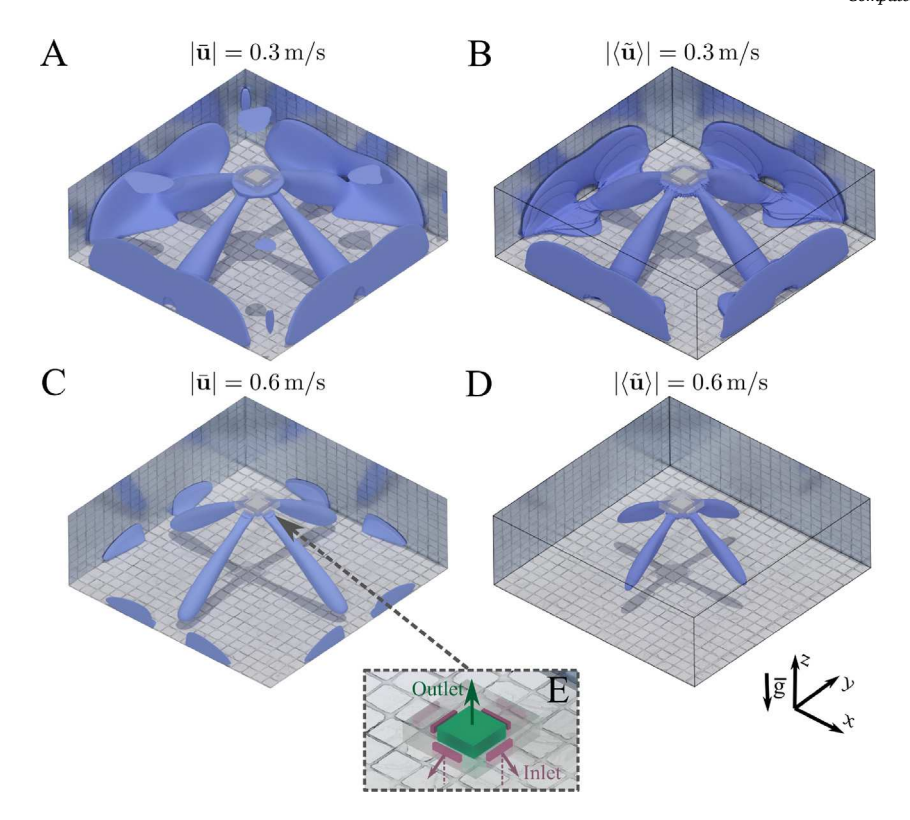


Fig. 1. Iso-surface of the velocity magnitude from RANS (panels A and C) and the temporally- and spatially-averaged velocity field from LES (panels B and D). The iso-surface value is shown at the top of each panel. (E) Enlarged view of the ventilation outlet and inlets located at the center of the ceiling.

As for boundary conditions, we impose the no-slip and nopenetration (i.e. zero velocity) condition on all the walls. The inlets and outlet are aligned with the ceiling. The outlet is set as a pressure outlet and the inlets are oriented at 40 deg with respect to the ceiling.

We take advantage of the one-way coupled nature of the problem [13] to use statistical overloading by initially placing a total of 1 million droplet nuclei ranging in diameter from 0.2 to 20  $\mu m$  (166,667 for each of the six nuclei sizes considered). While in the present simulations, we use one million nuclei, this is not representative of the volume fraction in a real situation and is only done for statistical overloading. In fact, for a single adult in the canonical room in question, the volume fraction of nuclei is usually on the order of  $10^{-6}$ . As such, the one-way coupling is adequate in this situation.

The flow is first allowed to reach a statistically stationary state, within which the droplet nuclei are uniformly but randomly placed within the room. The number of flow through times needed to reach the stationary state was approximately 3, where the flow through time was estimated as 3600/ACH. The large amount of droplet nuclei is consistent with what was used in [13] and is needed to provide statistically-relevant, ensemble-average results that account for the stochastic nature of turbulence.

The LES formulation was discussed in [13] and will be briefly summarized below. On the other hand, we will discuss the RANS formulation in more detail. Both the RANS and LES configurations consist of an Eulerian framework for the flow field and a Lagrangian framework for individually tracking droplet nuclei.

# 2.1. Mathematical formulation

**RANS Eulerian Flow Approach:** The flow field within the canonical room is solved for prior to solving for the Lagrangian particle trajectories. The flow is assumed to be turbulent and incompressible. Under

such assumptions, the unsteady governing RANS conservation equations for mass (Eq. (1)) and momentum (Eq. (2)) in their dimensional form can be defined as:

$$\frac{\partial \bar{u}_i}{\partial x_i} = 0,\tag{1}$$

$$\frac{\partial \bar{u}_i}{\partial t} + \bar{u}_j \frac{\partial \bar{u}_i}{\partial x_j} = -\frac{1}{\rho_f} \frac{\partial \bar{p}}{\partial x_i} + \frac{\mu_f}{\rho_f} \frac{\partial}{\partial x_j} \left( \frac{\partial \bar{u}_i}{\partial x_j} + \frac{\partial \bar{u}_j}{\partial x_i} - \frac{2}{3} \delta_{ij} \frac{\partial \bar{u}_l}{\partial x_l} \right) - \frac{\partial \overline{u_i' u_j'}}{\partial x_j}, (2)$$

where physical quantities with overbar indicate an ensemble average. In the above equation, i and j represent the direction indices,  $\bar{u}$  the three-dimensional flow velocity,  $u_i'$  the flow fluctuation velocity,  $\bar{p}$  the pressure,  $\rho_f$  the air density,  $\mu_f$  the air dynamic viscosity,  $\delta_{ij}$  the Kronecker delta function, and  $\overline{u_i'u_j'}$  the Reynolds stress. Based on the Boussinesq hypothesis, Eq. (3) is used to express the Reynolds stress in terms of the mean velocity gradients as follows [25]:

$$-\overline{u_i'u_j'} = \frac{\mu_t}{\rho_f} \left( \frac{\partial \bar{u}_i}{\partial x_j} + \frac{\partial \bar{u}_j}{\partial x_i} \right) - \frac{2}{3} \delta_{ij} \left( k + \frac{\mu_t}{\rho_f} \frac{\partial \bar{u}_l}{\partial x_l} \right), \tag{3}$$

where k represents the turbulent kinetic energy and  $\mu_t$  the turbulent viscosity, which must be modeled. We note that the first-order implicit scheme is used for time integration, the second-order upwind scheme is used for the advection terms, and the second-order centered scheme is used for the diffusion terms.

A structured grid is generated throughout the computational domain. Fine grids are generated near the walls to accurately capture the large flow gradients within the boundary layers as well as the turbulence statistics, while relatively coarse grids are generated away from the boundary regions. A grid dependency test is performed to ensure results are grid independent. The number of grid elements is varied from 4.4 million to 7.28 million (4.4, 5.13, 6.27 and 7.28 million). Velocity magnitudes along  $z=1.5\,\mathrm{m}$  and  $z=0.5\,\mathrm{m}$  are monitored for the different grids. As shown in Fig. 2, the resolution with 6.27 million grid points is observed to be adequate, and is thus adopted in the

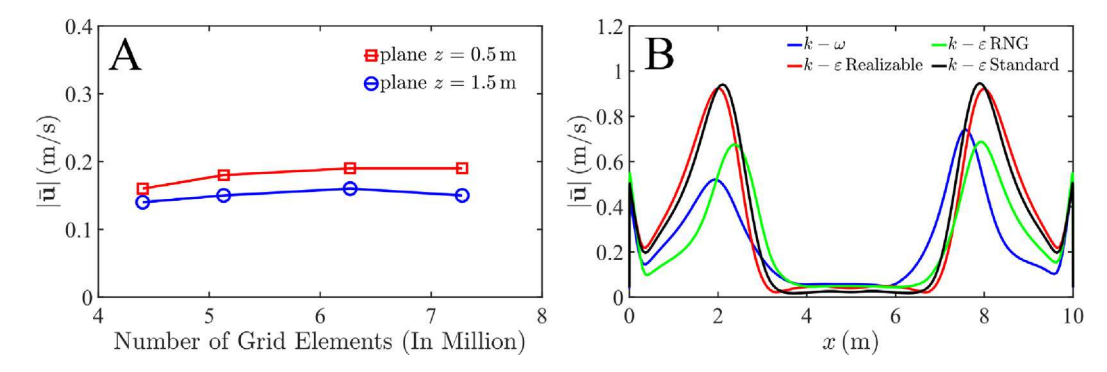


Fig. 2. (A) RANS mesh dependence study results based on plane average velocity magnitude. (B) RANS model dependence study results based on velocity magnitude along a line passing through intersection of the two planes v = 5 m and z = 0.5 m.

present paper. Furthermore, following a time-step independence study, the time step was chosen to be  $\Delta t = 0.5$  s. This time step is adequate and produces an approximate relative error below 1% when compared to a time step of 0.25 s. This insensitivity can be expected since in RANS we are solving for a stationary flow and not for a time-dependent flow.

In addition to the grid dependency test, a turbulence model dependency test is also carried out by considering four different turbulent models, namely  $k-\omega$ ,  $k-\varepsilon$  realizable,  $k-\varepsilon$  RNG and  $k-\varepsilon$  standard. The velocity magnitude distribution along the line defined by the intersection of the  $y = 5 \,\mathrm{m}$  and  $z = 0.5 \,\mathrm{m}$  planes is plotted for the different turbulence models. The  $k-\varepsilon$  realizable model and the  $k - \varepsilon$  standard model were both able to capture the inherent symmetry of the problem (see Fig. 2. While it is not our objective to claim superiority of one model over the other, the  $k-\varepsilon$  realizable model was adopted for the present paper. The realizable  $k - \varepsilon$  model is a relevant recent development and differs from the standard  $k - \varepsilon$  model in a few important ways [25]. The realizable  $k - \varepsilon$  model has been designed to satisfy certain mathematical constraints on the Reynolds stresses, consistent with the physics of turbulent flows. In the remainder of the paper, the realizable  $k - \varepsilon$  model, which has been rigorously tested [26-30] will be referred to as RANS2 for brevity.

Eqs. (4) and (5) represent the turbulence transport equations for the  $k - \varepsilon$  realizable model [25]:

$$\rho_{f} \frac{\partial k}{\partial t} + \rho_{f} \frac{\partial (k\bar{u}_{j})}{\partial x_{j}} = \frac{\partial}{\partial x_{j}} \left[ \left( \mu_{f} + \frac{\mu_{t}}{\sigma_{k}} \right) \frac{\partial k}{\partial x_{j}} \right] + G_{k} + G_{b} - \rho_{f} \varepsilon, \qquad (4)$$

$$\rho_{f} \frac{\partial \varepsilon}{\partial t} + \rho_{f} \frac{\partial (\varepsilon \bar{u}_{j})}{\partial x_{j}} = \frac{\partial}{\partial x_{j}} \left[ \left( \mu_{f} + \frac{\mu_{t}}{\sigma_{\varepsilon}} \right) \frac{\partial \varepsilon}{\partial x_{j}} \right] + \rho_{f} C_{1} (2S_{ij}S_{ij})^{1/2} \varepsilon$$

$$-\rho_{f} C_{2} \frac{\varepsilon^{2}}{k + \sqrt{(\mu_{f}/\rho_{f})\varepsilon}} + C_{1\varepsilon} \frac{\varepsilon}{k} C_{3\varepsilon} G_{b}, \qquad (5)$$

where,  $G_k$  and  $G_b$  represent turbulence kinetic energy generation by the mean velocity gradients and the buoyancy force, respectively.  $\sigma_{\varepsilon}$  and  $\sigma_k$  represent the Prandtl number based on the turbulent dissipation rate and the turbulent kinetic energy, respectively.  $C_1, C_2, C_{1\varepsilon}$  and  $C_{3\varepsilon}$  are constants,  $\varepsilon$  represents the turbulence dissipation rate, and  $S_{ij}$  represents the mean strain rate tensor.

The governing equations are solved using the finite volume method based software FLUENT 19.2, which employs the SIMPLE scheme and a second order upwind scheme for discretizing the convective terms. Furthermore, we implement an enhanced wall treatment of turbulence for the near-wall region [25] and use the pressure based solver PRESTO for solving the pressure equation.

The density  $(\rho_f)$  and dynamic viscosity  $(\mu_f)$  of air are kept constant with values of 1.2041 Kg/m³ and  $1.81\times 10^{-5}$  Ns/m². No slip boundary conditions are invoked at all the walls, and atmospheric conditions are enforced at the pressure outlet. Furthermore, we used a uniform inlet velocity profile, the magnitude of which varied from one simulation to the other, with values of 3.57, 7.14, and 14.28 m/s, corresponding to an ACH of 2.5, 5, and 10, respectively. The ACH values were chosen

to match those from the reference LES study [13]. In fact, the flow remains turbulent even at lower ACH values. Similar to the outlet, the four inlets lie in the plane of the ceiling, and each inlet has dimensions of  $5.5~\rm cm \times 44~\rm cm$ . The flow is angled downward and away from the outlet (see Fig. 1E) at an angle of  $40^{\circ}$  from the ceiling. Furthermore, the flow from each inlet is uniform, i.e. there is no variation of the flow within each inlet in terms of magnitude and orientation.

RANS Lagrangian Approach: Droplet nuclei trajectories are computed using the discrete phase method (DPM) available in FLUENT. In the Lagrangian framework, the path of each airborne nucleus is evaluated by solving the equations of motion. The nuclei volume fraction is assumed to be negligible so that nuclei neither affect the flow within the room, nor the trajectory of other nuclei through possible collisions. The only forces which are considered in the current study are the drag and gravitational forces. The resulting equation (6) for the particle velocity  $\mathbf{u}_n$  reads

$$\frac{d\mathbf{u}_p}{dt} = \frac{18\mu_f}{\rho_p d_p^2} \frac{C_D Re_p}{24} \left( \mathbf{u} - \mathbf{u}_p \right) + \frac{\mathbf{g} \left( \rho_p - \rho_f \right)}{\rho_p},\tag{6}$$

Here, **g** represents the gravitational acceleration vector,  $\rho_p$  and  $d_p$  the particle density and diameter,  $Re_p$  the particle Reynolds number, and  $C_D$  the drag coefficient.

The sub-micron-sized particles are modeled as tracer particles that follow the fluid flow with additional settling velocity. Therefore, the particle velocity of sub-micron-sized particles is evaluated as shown in Eq. (7):

$$\mathbf{u}_p = \mathbf{u} + \mathbf{V}_s,\tag{7}$$

where  ${\bf V}_s={\bf g}(\rho_p-\rho_f)d_p^2/(18\mu_f)$  is the still fluid settling velocity of nuclei and  ${\bf u}$  is the fluid velocity interpolated at the droplet nuclei location.

The RANS approach solves for only the ensemble-averaged velocity  $\bar{\mathbf{u}}$  and does not solve for the total fluid velocity including the turbulent perturbations. However, the instantaneous fluid velocity  $\mathbf{u}$ , that includes flow turbulence is required to accurately estimate the particle trajectories. The instantaneous fluid velocity is expressed in Eq. (8) as

$$\mathbf{u} = \bar{\mathbf{u}} + \mathbf{u}',\tag{8}$$

where the fluid velocity perturbation at the nuclei location (i.e.,  $\mathbf{u}'$ ) must be modeled. Here we use the continuous random walk (CRW) model based on the normalized Langevin equation [31].

The perturbation fluid velocity in the wall-normal (Eq. (9)) and the wall parallel (Eq. (10)) directions can be expressed as

$$u_2^{\prime n+1} = \frac{\sigma_2^{n+1}}{\sigma_2^n} u_2^{\prime n} \exp\left(-\frac{\Delta t}{\tau_2}\right) + \sigma_2^{n+1} \left(1 - \exp\left(-2\frac{\Delta t}{\tau_2}\right)\right)^{\frac{1}{2}} \lambda_2 + \frac{\sigma_2^{n+1} \tau_2}{1 + St_k} \frac{\partial \sigma_2^{n+1}}{\partial x_2} \left(1 - \exp\left(-\frac{\Delta t}{\tau_2}\right)\right), \tag{9}$$

$$u_i^{\prime n+1} = \frac{\sigma_i^{n+1}}{\sigma_i^n} u_i^{\prime n} \exp\left(-\frac{\Delta t}{\tau_i}\right) + \sigma_i^{n+1} \left(1 - \exp\left(-2\frac{\Delta t}{\tau_i}\right)\right)^{\frac{1}{2}} \lambda_i \tag{10}$$

where,  $\lambda_i$  is the zero mean unit variance Gaussian random number,  $St_k = \tau_p/\tau_L$  is the particle stokes number, where  $\tau_L$  is the Lagrangian fluid timescale, and  $\sigma_i$  is the Eulerian rms velocity fluctuation. The above equations can be used to evaluate the fluid velocity fluctuations along the nuclei trajectory at time level (n + 1) in terms of the velocity fluctuations at the earlier *n*th time level, where  $\Delta t$  is the gap between the two time levels. Also, the index 2 in Eq. (9) corresponds to the wall-normal direction, whereas the index i in Eq. (10) runs only over the wall-parallel directions. The third term on the right hand side of Eq. (9) corresponds to the mean drift correction in the wall normal direction, which is considered only in the near-wall region ( $y^+ \le$ 100). An additional finite-inertia correction coefficient  $(1/(1+St_k))$  is also considered to predict the proper concentration of nuclei near the walls and avoid spurious migration of submicron-sized nuclei towards the walls [31]. Furthermore, the drift term along the wall-parallel directions is neglected since only the velocity along the wall-normal direction has an impact on nuclei wall deposition [32].

Based on the findings of Bocksell and Loth [33], the time scales  $\tau_1, \tau_2, \tau_3$  are considered to be isotropic and equal to the Lagrangian time scale  $\tau_L$ . Following the literature [32], the Lagrangian time scale can be expressed as shown in Eqs. (11) through (13) as:

$$\tau_L = \frac{\mu_f}{\rho_f u^{*2}} \times 10 \qquad y^+ \le 5, \tag{11}$$

$$\tau_L = \frac{\mu_f}{\rho_f u^{*2}} \times \left(7.122 + 0.5731 y^+ - 0.00129 y^{+2}\right) \qquad 5 < y^+ \le 100, (12)$$

$$\tau_L = \frac{2}{C_0} \frac{k}{\varepsilon} \qquad \qquad y^+ > 100 \ . \tag{13}$$

Here  $y^+ = \rho_f y u^* / \mu_f$  represents the non-dimensional distance from the nearest wall in wall units,  $u^*$  corresponds to the friction velocity at the first grid cell, and  $C_0 = 14$  is a constant [34]. We note that around 95% of all grid points in the immediate vicinity of a wall have  $y^+$  < 1, and less than 1% of such grid points have  $y^+$  > 5. In order to track the nuclei motion based on the above-mentioned Lagrangian framework, the DPM capability of FLUENT is used with the particle time step size set to  $100 \mu s$ . Generally the particle time step is chosen to be smaller than the particle relaxation time  $(\tau_p=C_c\rho_pd_p^2/18\mu, \text{ here }C_c$  is Cunningham slip correction factor). For  $d_p=20~\mu\text{m},~\tau_p=1.24\times10^{-3}$  s, and for  $d_p=0.2~\mu\text{m},~\tau_p=2.31\times10^{-7}$  s. As noted by [35], for smaller nuclei, using a time step smaller than the relaxation time is not practical as it needlessly increases the computational cost. Owing to the small Stokes number of such small nuclei, the analytical equilibrium Eulerian velocity is used [36,37]. On the other hand, a time step larger than the relaxation time is employed for nuclei smaller than 1  $\mu m$ . A user defined function was developed for estimating the fluid perturbations using the aforementioned models. We should note that a nucleus is considered to have deposited on a wall when the distance between the nucleus center and the wall becomes less than the nucleus radius.

**LES formulation:** Only a brief summary of the LES formulation is provided here. Additional details can be found in [13]. The filtered large eddy incompressible equations for mass (Eq. (14)) and momentum (Eq. (15)) used for solving the air phase are given by [38].

$$\nabla \cdot \tilde{\mathbf{u}} = 0, \tag{14}$$

$$\frac{\partial \tilde{\mathbf{u}}}{\partial t} + \tilde{\mathbf{u}} \cdot \nabla \tilde{\mathbf{u}} = -\nabla \tilde{p} + (\nu + \nu_t) \nabla^2 \tilde{\mathbf{u}}. \tag{15}$$

The tilde here represents the filtered component of the variable. The eddy viscosity  $v_t$  is obtained using the dynamic Smagorinsky model to account for the sub-grid scale Reynolds stress. Each droplet nucleus is individually tracked using the equation of motion given for the RANS approach. Since turbulent eddies smaller than the grid size have been filtered, as in the RANS approach, the total fluid velocity at the nuclei location must be modeled as  $\mathbf{u} = \tilde{\mathbf{u}} + \mathbf{u}''$ . The resolved velocity  $\tilde{\mathbf{u}}$  represents the macroscale flow that is computed in the LES, and the subgrid

contribution  $\mathbf{u}''$  is computed using the Langevin model [31,32,39–41] as shown in Eq. (16)

$$\mathbf{u}'' \left[ \mathbf{X}_{l}(t + \Delta t), t + \Delta t \right] = \left[ 1 - \left( \frac{1}{2} + \frac{3C_{0}}{4} \right) \frac{C_{s}^{2} |\tilde{S}|}{2C_{Y}} \Delta t \right] \times \mathbf{u}'' \left[ \mathbf{X}_{l}(t), t \right] + \sqrt{C_{0}/3 \,\tilde{\epsilon} \Delta t} \, f_{w} \, \xi, \tag{16}$$

where  $\tilde{\epsilon} = v_t |\tilde{S}|^2$  is the dissipation rate that depends on the filtered strain rate tensor  $\tilde{S}$ .  $C_s$  corresponds to the dynamic Smagorinsky coefficient and  $\Delta t$  is the simulation time step. The wall filter function,  $f_w$ , reaches unity at distances over 100 wall units from any boundary, which accounts for the vast majority of the computational domain. At regions where the distance is below 100 wall units, this quantity falls below unity and approaches zero at the wall in an anisotropic manner [31]. The values of the parameters  $C_s = 0.18$ ,  $C_0 = 2.1$  and  $C_Y = 0.039$  are obtained from previous studies [42,43], and  $\xi \sim \mathcal{N}(0,1)$  is a Gaussian-distributed random variable. Since the RANS results are being compared with LES results, here we presented a very brief account of the LES method used, so that RANS/CRW can be properly compared.

# 3. Results and discussion

### 3.1. Flow comparison

In this section, we will compare the airflow computed in RANS2 against LES. Fig. 1 shows iso-surfaces of velocity magnitude obtained from RANS2 (panels A and C) and LES (panels B and D). For the LES data, in addition to time-averaging, the data has been spatiallyaveraged through the aforementioned 8-fold symmetry. We should stress here that the LES simulations are a function of time, however due to stationarity, the LES results were time-averaged and also eightfold spatially-averaged to approximate the ensemble average. The iso-surface plots depict the most important large-scale feature of the room-scale flow, consisting of the four jets extending from the respective inlets at the prescribed angle of 40°. The jets emanate from the inlets and remain fairly coherent until they hit the floor. Two values of the iso-surface are chosen, namely 0.3 and 0.6 m/s, and it can be seen that while both RANS2 and LES provide qualitatively similar results, the RANS2 jets are somewhat less diffusive, which is apparent in their longer and thicker profiles. The coherent nature of the jets in RANS2 is also apparent in the wall- and ceiling-rebounding flow. The iso-surface plots in Fig. 1 are for the simulation with ACH = 5. However, the plots scale linearly for the larger and smaller ACH simulations of 10 and 2.5.

Fig. 3 shows iso-contours of the velocity magnitude (top row of panels), of the vertical z-component of velocity (middle row of panels), and of the horizontal x-component of velocity (the bottom row of panels). The iso-contours are shown for the  $z=1.6\,\mathrm{m}$  plane. The velocity vectors within the  $z=1.6\,\mathrm{m}$  plane are also shown on top of the velocity contours in panel A for RANS2 and panel D for LES. The left column corresponds to RANS2, the center column to the time- and 8-fold-averaged LES, and the right column to instantaneous LES. The time instance at which the instantaneous snapshot in panels G, H, and I are extracted occurs at a time when the flow has reached a statistically stationary state. Clearly, a different time instance would give a different iso-contour, nonetheless the purpose of these instantaneous panels is to showcase the variability in the time-dependent LES simulations. We note here that the colormap is the same within each row, but does differ from one row to the other.

It is clear that the panels within each row are qualitatively very similar, and that the flow is dominated by the presence of the four jets. However, it is also clear that the contours are comparatively larger in RANS2 than they are in LES. For example, the peak velocity in panel A has a value of about 1.5 m/s compared to the LES value of approximately 0.9 m/s. Furthermore, as a result of the relatively strong and coherent flow in the jets as predicted by RANS2, we observe the rebounding flow on the sidewalls to be relatively thicker and more

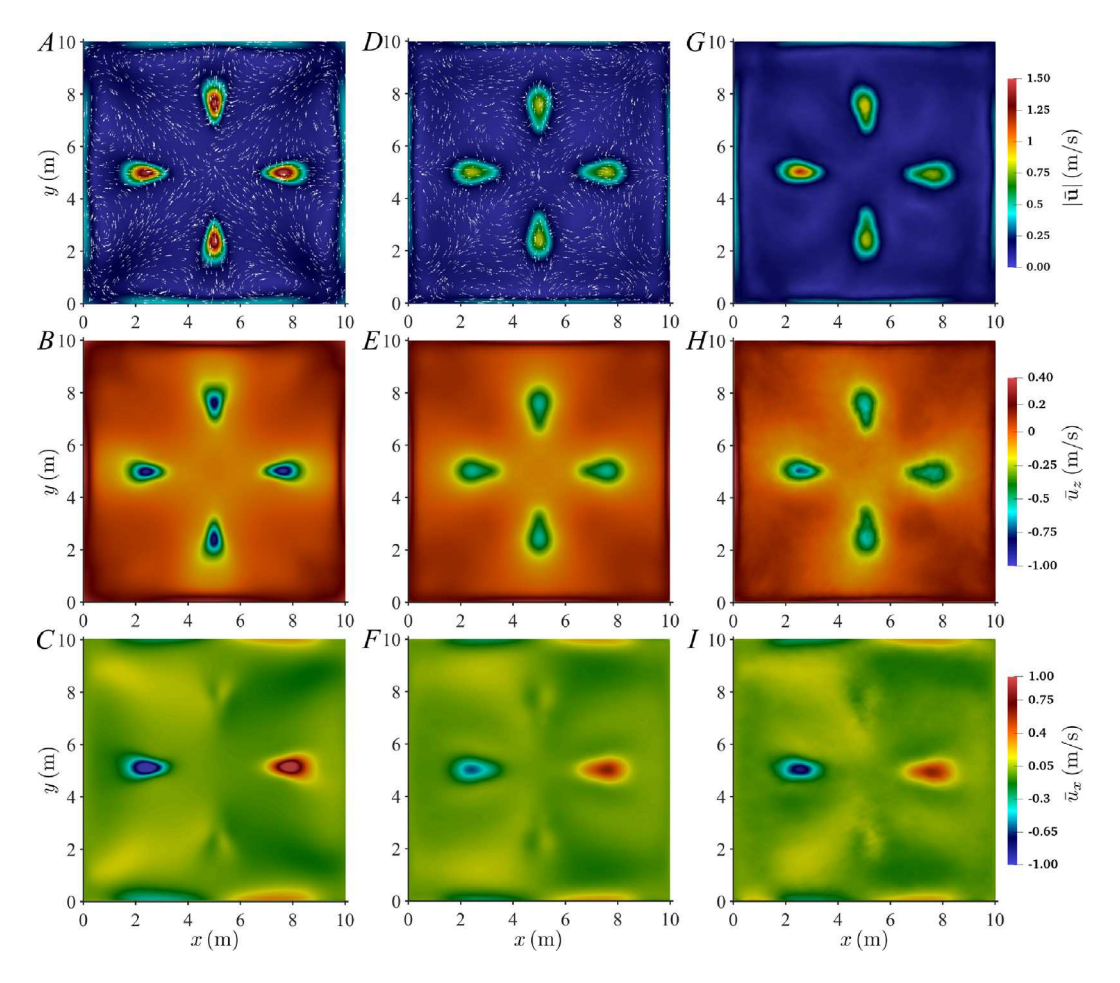


Fig. 3. Velocity iso-contours from RANS2 and LES at the  $z = 1.6 \,\mathrm{m}$  plane. (A) Velocity magnitude from RANS2. (B) z-component of velocity from RANS2. (C) x-component of velocity from RANS2. (D) Time and 8-fold spatially-averaged velocity magnitude from LES. (E) z-component of time and 8-fold spatially-averaged velocity from LES. (G) x-component of time-averaged 4-fold symmetric velocity from LES. (G) Instantaneous velocity magnitude from LES. (H) z-component of instantaneous velocity from LES. (I) x-component of Instantaneous velocity from LES.

intense compared to LES. On the other hand, we find the flow near the four corners to be weaker in RANS2 than in LES. However, for the majority of the room, we observe the flow to be much slower than in the path of the inlet jets with a velocity magnitude on the order of 0.1 m/s for the present case of ACH = 5. As far for the instantaneous snapshot from LES, we do observe occasional bursts where the jet velocity magnitude at z=1.6 exceeds 1.5 m/s. However, the flow remains qualitatively unchanged with four distinct tear-drop shaped jets aligned primarily along the respective axes.

It is interesting to note here that the cross-sectional shape of the jet has a teardrop shape at  $z=1.6\,\mathrm{m}$ , but that the major and minor axes of the teardrops are not aligned with the major and minor axes of the respective inlet (i.e. the axes have flipped). The flipping of axes, in which the cross-section of the jet has its major and minor axes switch orientation, is well-documented in elliptical and non-circular jets [44,45]. Thus, the change from the symmetric rectangular cross-section of the inlet to a non-symmetric teardrop shaped cross-section of the jet farther away is an interesting observation in the present context. Additionally, this flipping of axes has been also observed in non-canonical buoyancy-driven flows such as thermals [46] and gravity currents [47–49].

In panels B, E, and H, the iso-contours, which correspond to the vertical *z*-component of velocity, help to identify the large-scale motion within the room. The downward flow is observed to occur in a small portion of the room within and closely around the four jets, whereas for the majority of the room, the flow is directed upward. Consequently, the upward flow is much slower compared to the relatively intense,

downward-directed jets. As can be expected, the largest magnitude of the upward-directed flow occurs near the sidewalls. This behavior is quantitatively consistent between RANS2 and LES.

As for the horizontal component of velocity in panels C, F, and I, we again observe similar flow features between RANS2 and LES. The negative and positive horizontal velocities in the left and right teardrop shapes are due to the inclined orientation of the jets. However, it is interesting that there is a small but clearly identifiable horizontal component of velocity within the top and bottom teardrops that are along the  $x=5\,\mathrm{m}$  line. The outline of the teardrop can be easily identified across all three panels. We can also clearly observe that the x-component of velocity changes orientation from being positive in the right portion of the teardrop to being negative in the left portion of the teardrop. This behavior is again consistent across RANS2 and LES. This diverging flow behavior within the teardrop causes it to expand along its minor axis below the present horizontal plane of  $z=1.6\,\mathrm{m}$ .

Fig. 4 shows iso-contours of the velocity magnitude (top row of panels), the vertical z-component of velocity (middle row of panels), and the horizontal x-component of velocity (bottom row of panels). The iso-contours are shown in the x=5 m plane. The velocity vectors within the z=5 m plane are also shown on top of the velocity contours in panel A for RANS2 and panel D for LES. Together with the velocity vectors from Fig. 3, we can better identify the flow patterns. We observe a circulation cell that is bounded by the sidewall, the ceiling, and the inclined jet. This circulation cell can be identified in the upper corners in Fig. 4A and D. We can also observe that the impinging jet on the floor rebounds and creates pairs of counter-rotating circular cells in

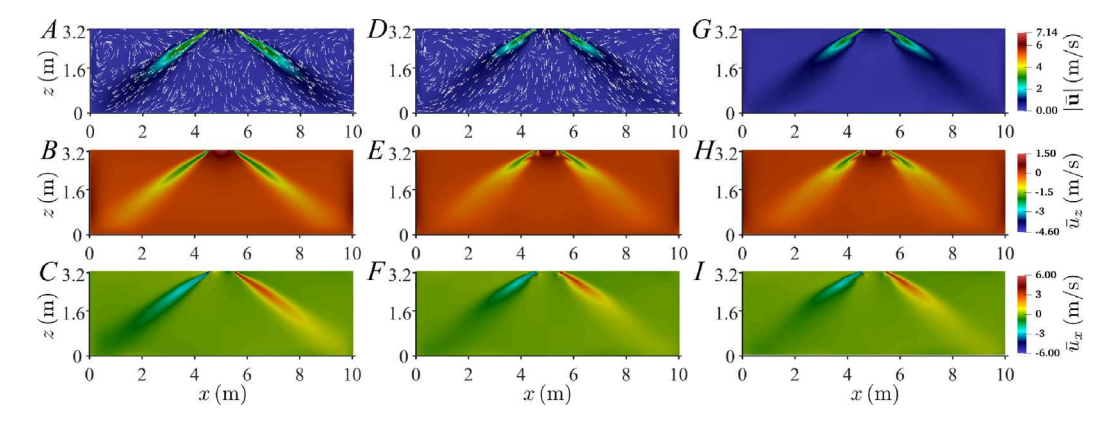


Fig. 4. Velocity iso-contours from RANS2 and LES at the y = 5 m plane. (A) Velocity magnitude from RANS2. (B) z-component of velocity from RANS2. (C) x-component of velocity from RANS2. (D) Time- and 4-fold spatially-averaged z-component of velocity from LES. (F) Time- and 4-fold spatially-averaged z-component of velocity from LES. (G) Instantaneous velocity magnitude from LES. (H) z-component of instantaneous velocity from LES. (I) x-component of instantaneous velocity from LES.

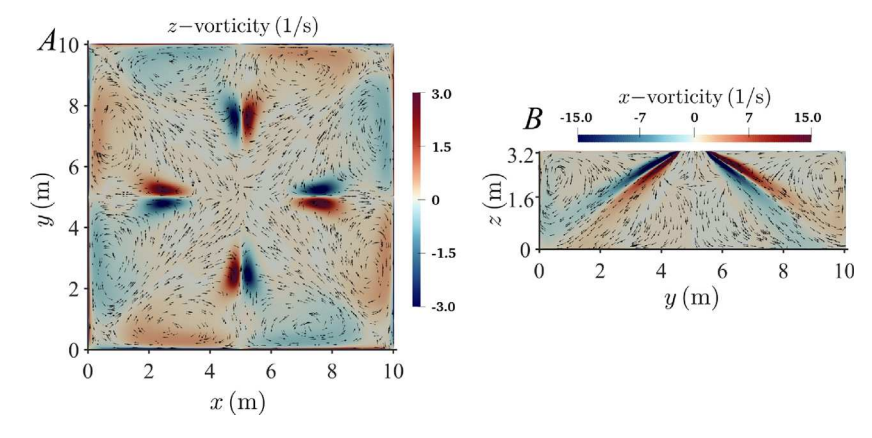


Fig. 5. Vorticity contours in the (A)  $z = 1.6 \,\mathrm{m}$  and (B)  $x = 5 \,\mathrm{m}$  planes. The contours are overlain with the respective velocity vectors in the plane in question.

the x-y plane. In fact, four such pairs can be identified from Fig. 3A and D. These counter rotating cells have a vertical z component and can be seen to be confined near the sidewalls where each pair of counter-rotating cells is roughly bisected by the room diagonal. Here as well, due to the symmetric nature of the problem, the x-component of velocity may be used to precisely infer the y-component of velocity, on the  $y=5\,\mathrm{m}$  plane. The results are similar across the RANS2 and LES simulations. The jets are initially very intense and narrow close to the inlets, however by around 50 cm from the ceiling, they are observed to span out due to entrainment [44,45]. We observe the RANS2 jets to remain more coherent and intense for a longer distance. One possible explanation is that with LES there is increased turbulent mixing and entrainment, which is not properly captured with RANS2. In the absence of such mixing, the jet penetration from RANS2 is observed to be longer than that from LES.

In RANS2, turbulent kinetic energy (TKE) is directly computed with the k equation, while in LES, TKE is computed as a post processing step through temporal and spatial averaging of the square of velocity fluctuation. In Fig. 6, we show iso-contours of TKE from RANS2 (left panels) and LES (right panels) in the  $z=1.6\,\mathrm{m}$  and  $x=5\,\mathrm{m}$  planes. The top panels (A and B) correspond to the horizontal plane of  $z=1.6\,\mathrm{m}$ , and the bottom panels (C and D) correspond to the vertical symmetry plane of  $x=5\,\mathrm{m}$ . While RANS2 reproduces the teardrop shape of the jet, we observe the peak values of TKE to be up to twice those from LES as shown in the panels A and B in the  $z=1.6\,\mathrm{m}$  plane. In the vertical slices, we observe the higher TKE values to extend farther towards the lower edge of the sidewalls in the case of RANS2. However, we find TKE to be locally large in LES, in the regions closer to the inlet. Away

from the jets, and over the majority of the room, TKE is more than an order of magnitude smaller both in RANS2 and LES.

A plot of the mean z and x components of vorticity from RANS2 is shown in Fig. 5. The contours for the z component are shown in the  $z=1.6\,\mathrm{m}$  plane in panel (A), and the contours for the x component are shown in the  $x=5\,\mathrm{m}$  plane in panel (B). The in-plane velocity vectors, composed of the x and y components for panel (A) and the y and z components for panel (B), are also shown in the figure to better identify the flow characteristics. The previously mentioned counterrotating cells in Fig. 3 are easily identified in panel (A). The vorticity magnitude is observed to be largest at the edge of the jets, and in the x- and y-aligned symmetry planes of the room. It is clearly also highest near the inlets, where the inlet speed is at its highest.

A quantitative comparison in terms of PDFs for the differences in velocity and TKE between RANS2 and LES is shown in Fig. 7. At each point within the domain the difference is computed and used to obtain the PDFs. The difference in velocity magnitude is shown in panel A, in the vertical z-component of velocity in panel B, in the horizontal x-component of velocity in panel C, and in TKE in panel D. The PDFs indicate that the range of differences for the considered case of ACH = 5 is on the order of  $0.1\,\mathrm{m/s}$  for velocity and on the order of  $0.01\,\mathrm{m^2/s^2}$  for TKE. From panel A, we do observe the PDF to be positively skewed with a mean velocity difference of  $2.3\times10^{-2}\,\mathrm{m/s}$ . The reason for the positive skewness is that the velocity magnitude differences are relatively large in the path of the jet in favor of RANS2. On the other hand, RANS2 under-predicts the velocity magnitude in some parts of the room, but the difference however is relatively small. This behavior is consistent with Figs. 3 and 4. We find all three components of velocity to have a

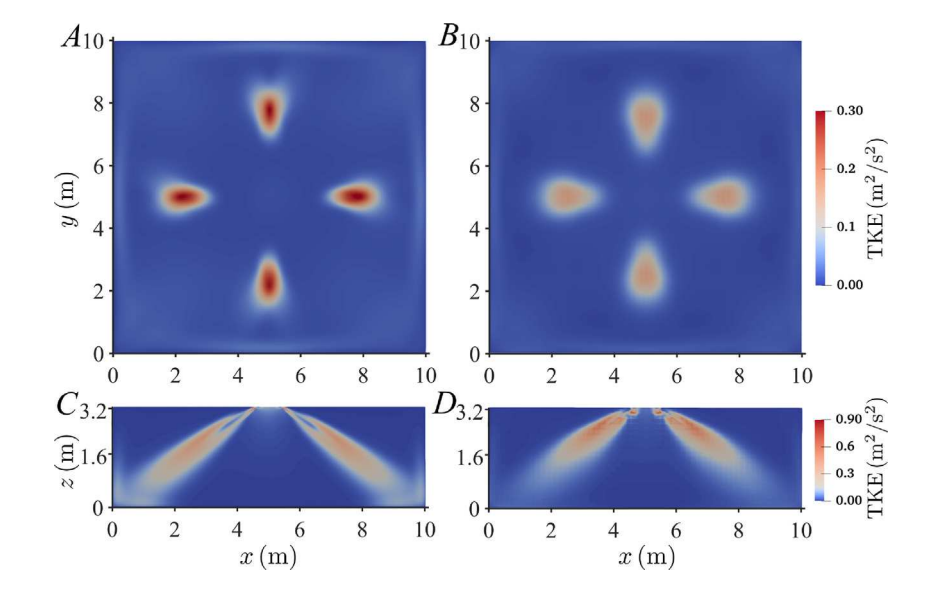


Fig. 6. TKE Iso-contour in the z = 1.6 m plane. (A) RANS2 TKE. (B) Time and 8-fold spatially-averaged TKE from LES. TKE Iso-contour in the y = 5 m plane (C) RANS2 TKE. (D) Time and 4-fold spatially-averaged TKE from LES.

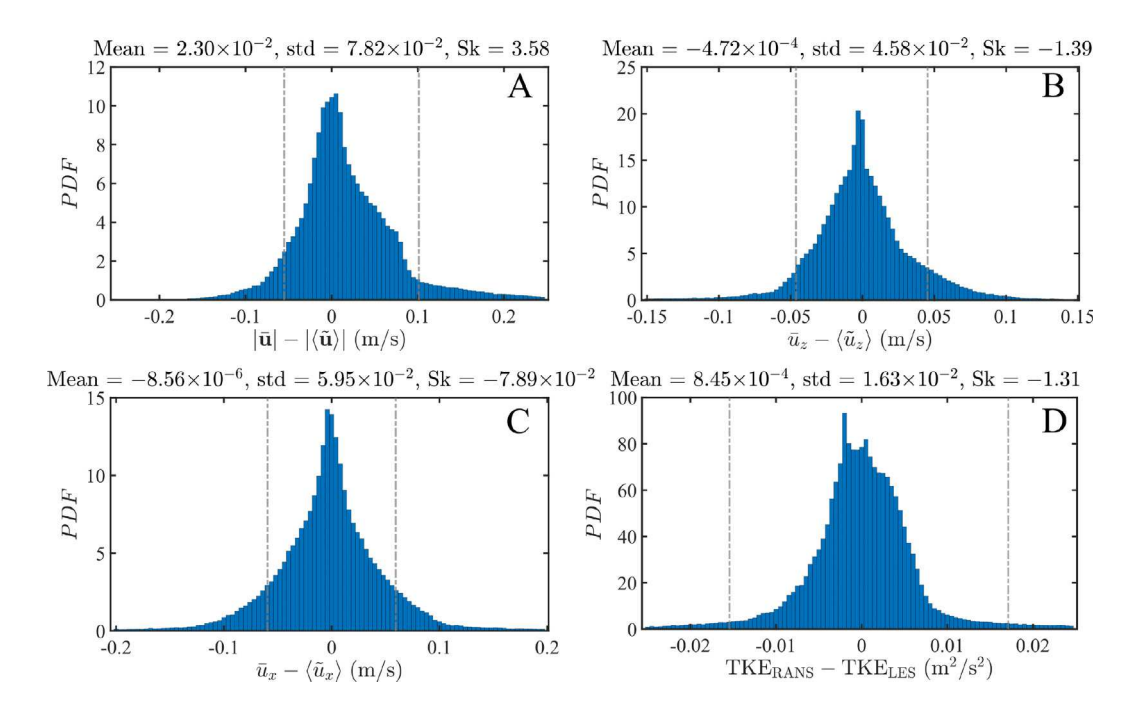


Fig. 7. PDFs of relative difference between RANS2 and LES. (A) PDF of relative difference of velocity magnitude between RANS2 and, time and 8-fold spatially-averaged LES in the entire domain. (B) PDF of relative difference of z-component of velocity between RANS2 and time and 8-fold spatially-averaged LES in the entire domain. (C) PDF of relative difference of x-component of velocity between RANS2 and temporally-averaged LES in the entire domain. (D) PDF of relative difference of TKE between RANS2 and time and 8-fold spatially-averaged LES in the entire domain.

nearly symmetric distribution. The mean values for the z and x components of velocity are  $-4.72\times10^{-4}$  m/s and  $-8.56\times10^{-6}$  m/s, respectively. The distribution for the x-component is expected to be symmetric by virtue of the symmetric nature of the problem. On the other hand, while RANS2 over-predicts the velocity in the jet, which is negative (i.e. it gives a more negative value of the z velocity difference), it over-predicts the magnitude in the rebounding flow near the sidewalls, which is positive. Similarly, we find the distribution for TKE to be nearly symmetric.

# 3.2. Droplet nuclei statistics

# 3.2.1. Room average statistics

Our main interest here is to explore the suitability of RANS in accurately predicting droplet nuclei concentration. Following [13], we will consider that an infected person (hereafter labeled source) may eject pathogen-laden droplet nuclei into the room at any location, and similarly that a receiver (hereafter labeled sink) be located anywhere in the room. Comparisons will be made at four levels: (i) the room average, which consists of averaging over all possible source locations

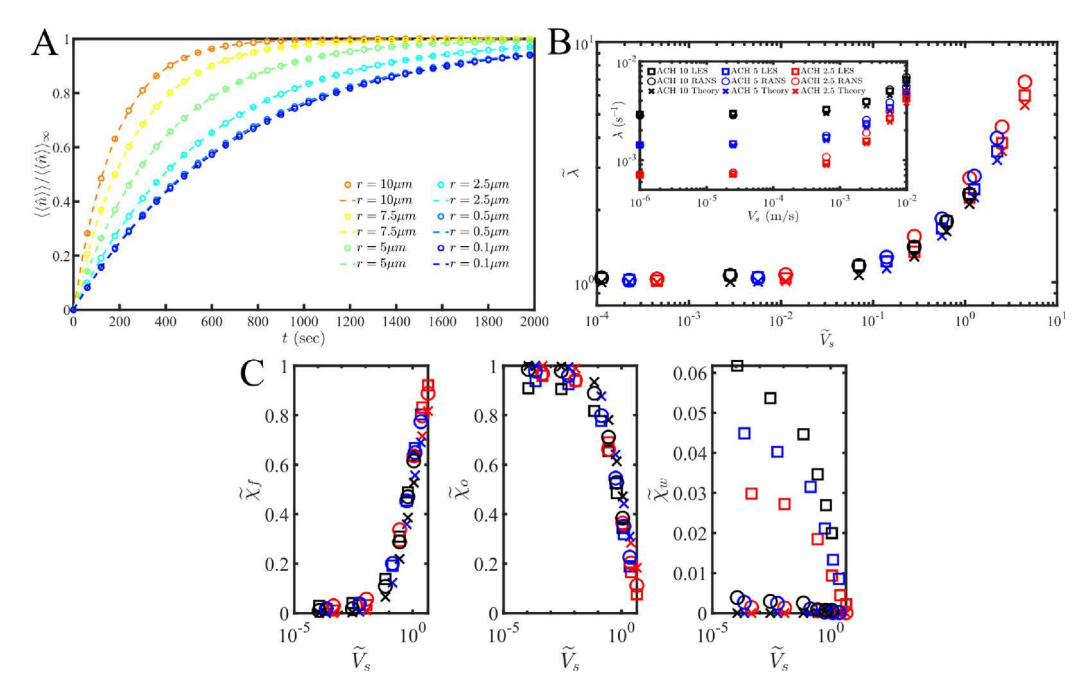


Fig. 8. (A) Variation of nuclei concentration vs time. RANS2 data 'o' vs exponential fit '-' for ACH = 5. (B) ACH-scaled exponential rate  $\tilde{\lambda}$  vs ACH-scaled settling velocity  $\widetilde{V}_i$ . Inset: Dimensional  $\lambda$  vs  $V_s$ . (C) Proportion of nuclei that exit through the floor  $(\tilde{\chi}_{\ell})$ , the outlet  $(\tilde{\chi}_{\theta})$ , and the walls  $(\tilde{\chi}_{w})$  relative to the total number of nuclei that were removed.

and all possible sink locations (this quantity can be compared with the well-mixed model), (ii) *the source average*, in which we average over all possible source locations so that the pathogen concentration can be given as a function of the sink location only, (iii) *the sink average*, in which we average over all possible sink locations so that the pathogen concentration can be given as a function of the source location only, and finally (iv) the average over all possible combinations of source-to-sink separation distances of 1, 2, 4, and 8 m.

We consider the case of an infected source entering the room at t = 0 and be located at the position  $\mathbf{x}_{so}$  within the room. Let the source be ejecting virus-laden droplets into the room due to activities such as breathing, talking, or singing. As the droplets evaporate and become airborne nuclei, their concentration within the room will continue to increase from the initial zero value before the arrival of the source. Over time the concentration of nuclei within the room will reach a constant value when the ejection rate by the source balances the rate of out-flux of nuclei. Nuclei can exit the room through the outlet, by settling to the floor, by deposition on the walls/ceiling, and by natural deactivation of the virus. Let  $\hat{n}(t, r, \mathbf{x}_{si}, \mathbf{x}_{so})$  be the time-dependent normalized concentration of nuclei of size r at the sink location  $\mathbf{x}_{si}$  that were emitted at the source location  $\mathbf{x}_{so}$ . Normalization is in terms of the rate at which the source is ejecting the droplet nuclei of size r per unit time. Thus, the time evolution of the concentration of droplet nuclei of size r at any point within the room due to a specific source can be evaluated by multiplying  $\hat{n}$  by the actual ejection rate of that nuclei size by the source. Thus,  $\hat{n}$  serves as a fundamental quantity that includes information about (i) all possible source locations and (ii) all possible sink locations and can be used to consider (iii) all possible ejection scenarios with proper scaling with the ejected droplet size spectra.

Fig. 8A shows the room-averaged (i.e., averaged over all source and sink locations) nuclei concentration  $\langle\langle\hat{n}\rangle\rangle$  for the six different nuclei sizes of 0.1, 0.5, 2.5, 5, 7.5, and 10  $\mu m$ . The normalized concentration of each nuclei size is further scaled by the respective steady-state nuclei concentration  $\langle\langle\hat{n}\rangle\rangle_{\infty}$ . The circular symbols correspond to the RANS2 data and the dashed lines represent the exponential fitting curves of the form shown in Eq. (17)

$$\frac{\langle\langle\hat{n}\rangle\rangle}{\langle\langle\hat{n}\rangle\rangle_{cs}} = 1 - \exp\left(-\lambda t\right),\tag{17}$$

where  $\lambda$  is the exponential rate shown in the inset of Fig. 8B for the six different nuclei sizes from the three different ACH simulations of 2.5 (red symbols), 5 (blue symbols), and 10 (black symbols). The value of  $\lambda$  is observed to increase with nuclei size indicating that these nuclei exit the room at a faster rate compared to the smaller nuclei.

In Fig. 8B, we plot the values of  $\lambda$  from the RANS2 (circle symbols) and LES (square symbols) simulations as well as from the well-mixed model (cross symbols) against the respective settling velocity  $V_s$  for each size. According to the well-mixed model, the exponential rate can be predicted by Eq. (18)

$$\lambda_{wm}(r) = \frac{Q}{\mathcal{V}} + \frac{V_s(r)}{H} + \lambda_{dep}(r) + \lambda_{da}. \tag{18}$$

The first term on the right-hand side accounts for exit through the air outlet, where Q is the air flow rate in and out of the room by the air conditioner,  $\mathcal{V}$  the room volume, and H the room height. Note that air changes per hour is then given by ACH/3600 =  $Q/\mathcal{V}$ . The other three terms account for gravitational settling, deposition on the walls/ceiling, and viral deactivation, respectively. We find generally good agreement between the RANS2 and LES results with differences ranging from 0.64% (for ACH = 5) for the smallest size of  $r = 0.1 \, \mu \text{m}$  to about 13.4% (for ACH = 5) for the largest size of  $r = 10 \, \mu \text{m}$ . We also observe as reported in [13] that when normalized by ACH, the exponential rate versus settling velocity collapses onto a single curve (i.e. the effect of ACH can be factored out). Here the non-dimensional exponential rate and settling velocity (Eq. (19)) are given by [13]

$$\tilde{\lambda} = \lambda \frac{3600}{\text{ACH}} \qquad ; \qquad \tilde{V}_s = V_s \frac{3600}{\text{ACH } H}. \tag{19}$$

Furthermore, we note the following in regards to the excellent agreement in the values of the exponential rates  $\lambda$  for smaller nuclei and the larger differences for larger nuclei. Both RANS2 and LES show excellent agreement with the well-mixed model for the small nuclei. This excellent agreement (on the order of 1%) is an indication of the well-mixedness of small nuclei in the room. The concentration of fairly well-mixed small nuclei is predominantly determined by the rate at which they are continuously removed from the room through the outlet. The other two modes of removal, namely gravitational settling and turbulent wall deposition constitute a small fraction compared to removal by the outlet. Therefore, the details of how well the nuclei

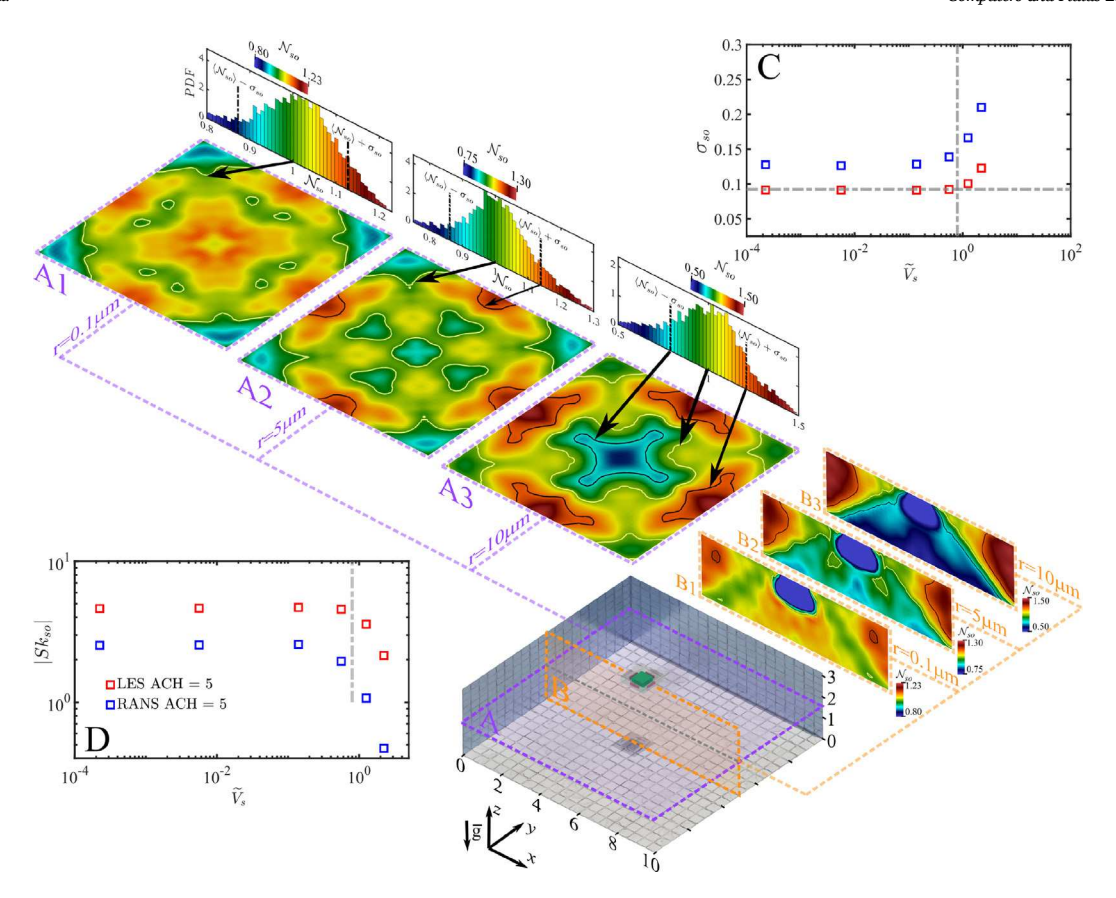


Fig. 9. Concentration from the source's perspective. For the ACH = 5 case, composite plot of contours of  $\mathcal{N}_{so}$  at (A) z=1.5m (violet planes) and (B) y=5m (orange planes), for different nuclei sizes (A1–A3 and B1–B3). Also, for planes A1 to A3, we show the probability density function (PDF) for the scaled concentration  $\mathcal{N}_{so}$  for each nuclei size in the entire room. Note that the PDFs and contour plots are colored by values of  $\mathcal{N}_{so}$ . Furthermore, the insets show (C) the standard deviation  $\sigma_{so}$  and (D) absolute value of skewness  $|Sk_{so}|$  of the PDFs as a function of scaled settling  $\widetilde{V}_{so}$ , for all cases.

are mixed in RANS2 vs LES matters less. On the other hand, for relatively large nuclei, gravitational settling is the dominant mode of removal. Moreover, the non-linear nature of the drag model coupled with the turbulent fluctuations in LES (that are non-existent in RANS) can modify gravitational settling and consequently the exponential rate  $\lambda$ .

Finally, in Fig. 8C we plot the portion of the nuclei that exit through the floor  $\widetilde{\chi}_f$ , the outlet  $\widetilde{\chi}_o$ , and the sidewalls and ceiling  $\widetilde{\chi}_f$  versus the non-dimensional settling velocity  $\widetilde{V}_s$ . By definition,  $\widetilde{\chi}_f + \widetilde{\chi}_o + \widetilde{\chi}_w = 1$ (here exit by viral deactivation has been ignored). Again, we observe very good collapse across all three ACH values. This collapse implies that droplet nuclei of size 10 µm in a room subjected to a ventilation flow rate of ACH = 5 would have an exponential rate  $\tilde{\lambda}$  that is similar to droplet nuclei of larger (respectively smaller) size when subjected to a larger (respectively smaller) ACH value. Similarly, the exit mechanism in terms of the portion of the nuclei that exit through the floor, the sidewalls and the ceiling, or the outlet would also scale similarly. While there are large differences in the rightmost plot in panel C, it should be noted that the scale of the vertical axis (i.e. of  $\tilde{\chi}_w$ ) is very small. The plots in panel C indicate that the main exit mechanism for small droplet nuclei is through the outlet, and for large droplet nuclei through settling to the floor. We observe very little turbulent deposition on the sidewalls, where the LES prediction is consistently higher.

At the present level of room average, the major conclusions are as follows: RANS2 simulations are well-suited to predict the exponential rate and exit mechanisms of the airborne droplet nuclei. More specifically, differences in the exponential rates  $\lambda$  can be as small as a fraction of a percent for sub-micron nuclei and as large as 13% for nuclei on the order of 10 microns for an ACH of 2.5. Similarly, both the room-averaged RANS2 and LES results are well predicted by the well-mixed model for sub-micron

nuclei. The well-mixed model however underpredicts the exponential rate for larger nuclei.

# 3.2.2. Sink-averaged statistics

Next we investigate the nuclei concentration from the source perspective by averaging over all possible sink locations. This is the scenario in which the precise location of the source may be known or specified, but the sink may be at any location (i.e. the receiving host may sit anywhere in the room with equal probability). Such a scenario could correspond to a classroom where the instructor is lecturing from a fixed position and the pathogen concentration emitted from the instructor is of interest. This scenario would provide the risk of airborne transmission to the students (whose location can be anywhere) depending on the instructor's location.

Fig. 9 shows iso-contours at steady-state (i.e., for  $t \to \infty$ ) of the sinkaveraged nuclei concentration as a function of source location obtained by averaging the ACH = 5 RANS2 results. The contours are shown for r = 0.1, 5, and 10  $\mu$ m in the horizontal plane of z = 1.6 m and the vertical symmetry plane of  $y = 5 \,\mathrm{m}$ . These planes are depicted as the purple and orange planes in the three-dimensional isometric view of the room, respectively. The contour plots may be understood as follows. For the case of the  $r = 0.1 \,\mu\text{m}$ , should the source be located within the red-colored regions (i.e., near the sidewalls and towards the center of the room, for example) then the concentration of virus-laden nuclei averaged over all possible sink locations would be higher than the room average. Correspondingly, if the source where to be located in the blue regions (such as in the corners), then the sink-averaged concentration will be lower than the room-average. The same analysis is true for the other two nuclei sizes of  $r = 5 \,\mu \text{m}$  and  $r = 10 \,\mu \text{m}$ . Thus, the blue regions are ideal spots for the source to be located in order

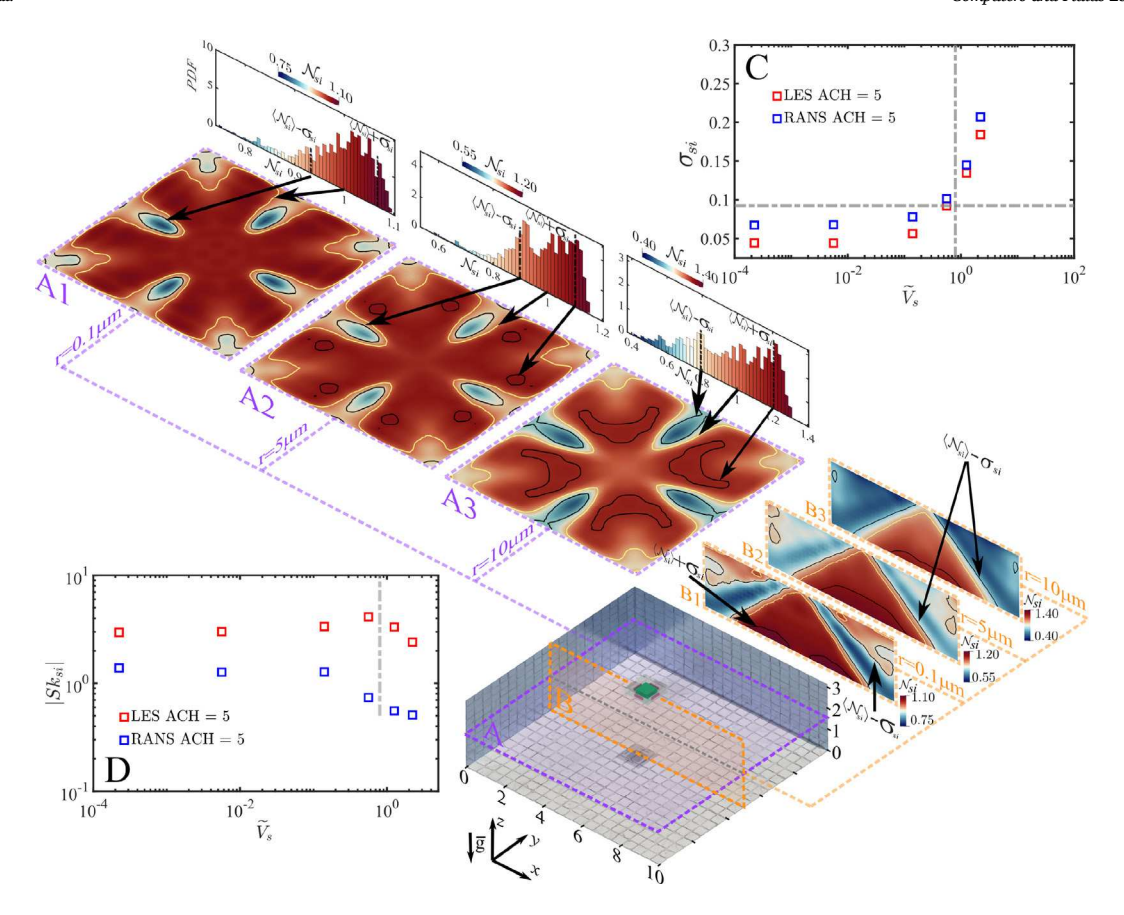


Fig. 10. Concentration from the receiver's perspective. For the ACH = 5 case, composite plot of contours of  $\mathcal{N}_{si}$  at (A) z=1.5m (violet planes) and (B) y=5m (orange planes), for different nuclei sizes (A1-A3 and B1-B3). Also, for planes A1 to A3, we show the probability density function (PDF) for the scaled concentration  $\mathcal{N}_{si}$  for each nuclei size in the entire room. Note that the PDFs and contour plots are colored by values of  $\mathcal{N}_{si}$ . Furthermore, the insets show (C) the standard deviation  $\sigma_{si}$  and (D) absolute value of skewness  $|Sk_{si}|$  of the PDFs as a function of scaled settling  $\widetilde{V}_{si}$ , for all cases.

to minimize the average risk of contagion. Based on this reasoning, it may be appropriate to place an infected person in the corner regions of the room, since the corresponding sink-averaged concentration is low for all nuclei sizes.

Additionally, for each of the three droplet nuclei sizes, we plot the PDF of sink-averaged concentration for all source locations within the room. It can be observed that the range of concentrations increases as the nuclei size increases. For example, for the  $r = 0.1 \, \mu \text{m}$  size the sinkaveraged concentration varies between 0.80 and 1.23, whereas for the  $r = 5 \,\mu\text{m}$  and the  $r = 10 \,\mu\text{m}$  size, the sink-averaged concentration  $N_{so}$ varies between 0.75 and 1.3, and 0.5 and 1.5, respectively. The smaller variation indicates that the concentration everywhere within the room is close to the room average, whereas larger variations indicate that there are regions where the concentration is much higher (or lower) than the room average. Similar results for the LES were reported in [13] and we note that the contour plots presented in Fig. 9 for RANS2 are quite similar to those from LES. In panels C and D, we plot the standard deviation and skewness of the PDF in the entire room for all six nuclei sizes from both RANS2 and LES against the non-dimensional settling velocity. We observe the standard deviation  $\sigma_{so}$  to be consistently larger in RANS2 compared to LES, on the other hand we find the absolute value of the skewness  $|Sk_{so}|$  to be consistently smaller in RANS2 compared to LES.

# 3.2.3. Source-averaged statistics

In this section, we investigate the complementary scenario of sourceaveraged statistics, which will help answer the important question of where in the room should a receiving host (sink) be located in order to minimize the risk of contagion if the location of the source (i.e., the infected person) is not known and therefore must be assumed to be anywhere in the room with equal probability. Towards this goal, we average the normalized nuclei concentration  $\hat{n}$  over all possible source locations  $\mathbf{x}_{so}$  and present the results primarily as a function of the sink location  $\mathbf{x}_{si}$  and time for the different nuclei sizes.

Fig. 10 shows iso-contours at steady-state of the source-averaged nuclei concentration as a function of sink location. The case being considered is again the ACH = 5 RANS2 simulation with three droplet nuclei sizes, namely r = 0.1, 5, and 10  $\mu$ m. The contours are shown in the horizontal plane of  $z = 1.6 \,\mathrm{m}$  and the vertical symmetry plane of  $y = 5 \,\mathrm{m}$ . The contour plots may be understood as follows. For the case of the  $r = 0.1 \,\mu\text{m}$ , should the sink be located within the dark red colored regions (which cover the room center and adjacent to the room corners) then the nuclei concentration averaged over all possible source locations would be higher than the room average. On the other hand, if the sink where to be located in the blue regions (i.e., in the path of the jets or in the corners) the nuclei concentration will be lower than the room average. The same analysis is true for the other two nuclei sizes of  $r=5\,\mu\mathrm{m}$  and  $r=10\,\mu\mathrm{m}$ . Based on these results, it may be optimal for an individual to locate oneself either in the corners or in the path of the jets to reduce the risk of infection. These RANS2 results are also qualitatively consistent with the corresponding findings of the LES presented in [13].

Additionally, for each of the three droplet nuclei sizes, we plot the PDF of the source-averaged concentration based on the sink location. Here again, it can be observed that the range of concentrations increases as the nuclei size increases. For example, for the  $r=0.1\,\mu\mathrm{m}$  size, the source-averaged concentration  $N_{si}$  varies between 0.75 and 1.1, whereas for the  $r=5\,\mu\mathrm{m}$  and the  $r=10\,\mu\mathrm{m}$  size the source-averaged concentration  $N_{si}$  varies between 0.55 and 1.2, and 0.4 and 1.4, respectively. The smaller variation for the smaller nuclei indicates

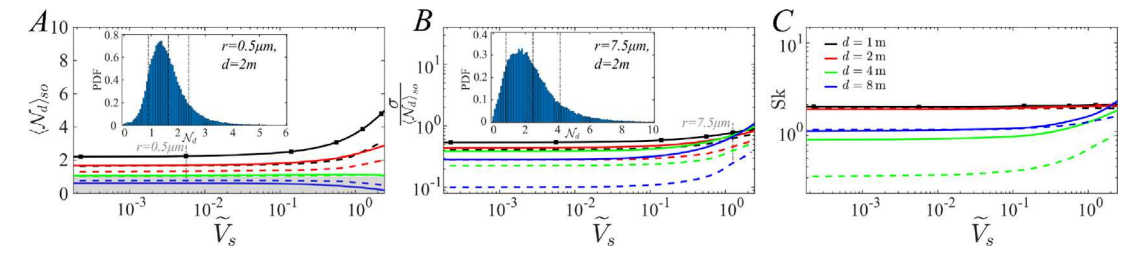


Fig. 11. (A) Average concentration  $\langle N_d \rangle_{so}$  at the sink location versus non-dimensional settling velocity  $\widetilde{V}_s$  for all possible source-to-sink separation distances of 1 m (black), 2 m (red), 4 m (green), and 8 m (blue) from RANS2 (solid curves) and LES (dashed curves).  $\langle N_d \rangle_{so}$  is normalized by the room-averaged concentration. Inset: PDF form RANS2 for the specific case of d=2 m and r=0.5 μm. (B) Same as (A) but for the standard deviation  $\sigma$ . Inset: Same as the inset in (A) but for r=7.5 μm. (C) Same as A but for skewness.

that their concentration anywhere within the room is reasonably close to the room average. In panels C and D, we plot the standard deviation and skewness of the PDF for all six nuclei sizes obtained from both RANS2 and LES against the non-dimensional settling velocity for the case of ACH = 5. We observe the standard deviation  $\sigma_{si}$  to be consistently larger in RANS2 compared to LES and the absolute value of the skewness  $|Sk_{si}|$  to be consistently smaller in RANS2 compared to LES.

#### 3.2.4. Statistics for fixed source-to-sink separations

A principal interest in social distancing is to maintain a specific separation between individuals so as to lower the risk of infection. The idea is that as people get farther away from one another, the likely concentration of droplet nuclei that one would be subjected to would be lower than had they been closer to one another. A main deficiency in the well-mixed model is that it does not recognize this source-to-sink separation as a key parameter affecting pathogen concentration. In fact, as far as the well-mixed model is concerned, being 6 ft or 60 ft apart makes no difference since droplet nuclei are assumed to perfectly and instantaneously well mix within the room and therefore are equally available to everyone independent of their relative location [12]. Salinas et al. (2022) [13] showed that the pathogen concentration received from a sink depends strongly on the source-to-sink separation.

In order to quantify the effect of source-to-sink separation distance, in this section we average the normalized nuclei concentration  $\hat{n}$  over all possible locations of source and sink within the room, such that they are separated exactly by a distance d. In Fig. 11, we plot the mean, standard deviation, and skewness of the PDF of nuclei concentration for separation distances of d=1,2,4, and 8 m, for the six different nuclei sizes. In the main frame of panel A, we plot the mean concentration  $\langle \hat{N}_d \rangle_{so}$ , scaled by the well-mixed concentration, from RANS2 (solid lines) and LES (dashed lines). The three main frames present the average, standard deviation, and skewness of nuclei concentration obtained for specific nuclei size and source-to-sink distance. The results are plotted against the non-dimensional settling velocity such that the results become independent of the value of ACH.

The RANS2 results qualitatively follow the same LES trends for all three statistics. In other words, RANS2 is able to capture the behavior of the leading-order average statistics and the higher-order statistics of standard deviation and skewness. However, we observe the predicted concentration from RANS2 to be consistently larger compared to LES. While RANS2 over-predicts the nuclei concentration at shorter distances, it is observed to under-predict the concentration at larger distances (i.e. the blue dashed line in panel A, which represents the  $d = 8 \,\mathrm{m}$  separation, is above the blue solid line). Furthermore, the grey-shaded rectangular area at the bottom of the main panel in A is representative of the concentration predicted by the well-mixed model, which is independent of d. Curves that lie within the shaded region (the blue curve in the present case) indicate that the concentration is below that predicted by the well-mixed model, and vice versa. Additionally, in the inset of panel A, we show the PDF of nuclei concentration for  $d=2\,\mathrm{m}$  and  $r=0.5\,\mathrm{\mu m}$ . Data from this PDF was used to extract the corresponding data points in the main frame. For the present case of d = 2 m and r = 0.5 um, this data consisted of the average concentration of 1.64, the standard deviation of 0.75, and the skewness of 1.79. The corresponding LES values are 1.34, 0.37, and 1.79, respectively.

# 3.2.5. Correction to the well-mixed model

The well-mixed model, despite its shortcomings, remains a useful tool for assessing the risk of contagion in confined spaces. As previously mentioned, the utility of the well-mixed model can be enhanced by incorporating the effect of source-sink separation distance. Salinas et al. (2022) [13] proposed a simple correction function  $\gamma(t,d)$  that could be straightforwardly used in conjunction with the well-mixed model to provide accurate predictions by incorporating the effect of a specific source-to-sink separation distance. More specifically, if we denote the cumulative exposure time (CET) predicted by the wellmixed model to be  $(N\tau)_{um}$ , where N is the number of occupants of the room and  $\tau$  is the safe exposure time for a chosen level of risk (see [12,13]), then the corrected CET can be expressed as  $(N\tau)$  =  $(N\tau)_{wm}/\gamma$ . Thus a  $\gamma$  greater (or smaller) than unity will reduce (or increase) the cumulative exposure time to account for the increase (or decrease) in nuclei concentration at shorter (or longer) separation distances. The correction function  $\gamma$  is also a function of the expiratory activity, i.e. breathing, singing, talking, etc. and of ACH. However, [13] showed that the dependence on expiratory activity and ACH is very weak and may be ignored for practical purposes.

Fig. 12A shows the asymptotic value of the correction function  $\gamma_{\infty}(d) = \gamma(t \to \infty, d)$ . The solid curves represent the RANS2 data, and the dashed curves the LES data. Both sets of curves confirm the weak dependence on expiratory activity. In the case of RANS2, at a distance of d=2 m,  $\gamma_{\infty}\approx 1.8$  (for mouth breating) indicates that on average if the well-mixed model would predict a safe exposure time of T minutes, then for individuals who are adhering to a separation of two meters, the safe exposure time should be modified to T/1.8. On the other hand, if individuals are adhering to a larger separation of eight meters for example, then the safe exposure time should be relaxed to T/0.5. Here again, RANS2 is able to capture the same decreasing trend of  $\gamma_{\infty}$ as a function of separation distance d. However, it is comparatively overly-restrictive at distances below 4 m and overly-relaxed for larger distances. This difference between RANS2 and LES may be explained as follows: For larger source-to-sink separations, we observe the concentration at the sink from RANS to be smaller than that observed in LES. The turbulent fluctuations in LES could provide a means to transport the larger nuclei over longer distances. Such fluctuations are not present in RANS and could explain the above observation. This inability to transport to farther distances also contributes to higher concentration at shorter distances.

In Fig. 12B, we plot the time-dependence of the correction function. Here we observe that for a short time duration, the correction function can be as large as 15 for short separation distances on the order of 1 m. As time increases, the time-dependent correction function  $\gamma$  tends to the steady state value  $\gamma_{\infty}$ . Once again, the trends are very well captured in RANS2. The peaks for d=1 and 2 m vary only by a few percent both in magnitude and in time of occurrence with respect to LES. Moreover, we find that RANS2 correctly predicts a local maximum for the aforementioned d values of 1 and 2 m, and the lack of a maximum over larger separations.

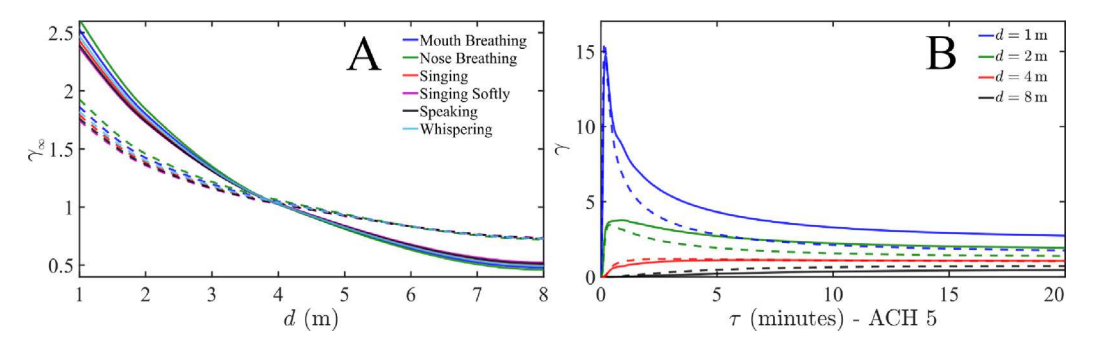


**Fig. 12.** (A) Steady-state correction function as a function of source-to-sink distance for different expiratory activities for ACH = 5 from RANS2 (solid curves) and LES (dashed curves). (B) Time-dependent correction function for ACH = 5 as a function of exposure time for distances of d = 1m (blue), 2 m (green), 4 m (red), and 8 m (black) from RANS2 (solid curves) and LES (dashed curves).

#### 4. Summary and conclusions

We conducted three RANS simulations to investigate the dispersal of droplet nuclei inside a canonical room of size  $10\times10\times3.2\,\mathrm{m}^3$ . The room had a four-way cassette air-conditioning unit installed at the center of the ceiling. Each of the three simulations corresponded to a particular air changes per hour (ACH) value of 2.5, 5, or 10. We employed statistical overloading where a total of one million droplet nuclei of size ranging from 0.1 to 10  $\mu m$  were initially uniformly but randomly placed inside the room. The nuclei were split into 6 sizes (166,667 nuclei per size) and were individually tracked for the entire duration of the simulation or until they were removed by the ventilation outlet or had deposited on the floor or walls. The size of the room as well as the operating conditions were chosen to match a recent high-fidelity large eddy simulation (LES) study.

One of the main objectives of this paper is to assess the suitability of RANS in predicting pathogen concentration within confined spaces. Out of four different RANS models, we chose the  $k-\varepsilon$  realizable model (referenced as RANS2 in the present paper) and compared flow and particle statistics between the present RANS simulations and the reference LES simulations. For the flow field, we find that RANS2 was able to qualitatively reproduce the same flow patterns observed in LES. Nonetheless, we did observe some discrepancy, namely that the inlet jets emanating from the air-conditioning unit remained more coherent and had a longer penetration depth in RANS.

The RANS droplet statistics were compared to LES at three different levels: (i) room average, (ii) average over all possible source locations (referred to as source-averaged statistics) or average over all possible receiving host (sink) locations (referred to as sink-averaged statistics), and (iii) average over all source-to-sink combinations of specific separation. For the room-averaged statistics, and for sub-micron nuclei, the agreement is excellent with differences on the order of a fraction of a percent. However, for larger nuclei, the difference between RANS and LES predictions increase. For example, for nuclei of radius 10  $\mu m$  and at an ACH of 2.5, the difference between RANS2 and LES is around 13.6%. For smaller nuclei, or for larger ACH values, the difference is usually around a few percent.

For the source-averaged and for the sink-averaged statistics, both RANS2 and LES predict that the safest location for a potentially sick individual, when the location of the receiving host is unrestricted or unknown, to be in the corners of the room. Similarly, both RANS2 and LES predict the safest location within the room, when the location of the sick individual is unrestricted or unknown, to be in the path of the jets. As for the average over specific separation distances of 1, 2, 4, and 8 m, RANS2 was able to correctly reproduce the trend in pathogen concentration. There were however quantitative differences that varied with separation distance and nuclei size on the order of 20%. It was however remarkable that RANS2 was able to capture the correct trends of the zeroth and higher-order statistics of pathogen concentration.

These statistics include the mean, standard deviation, and skewness of nuclei concentration for source-to-sink distances of 1, 2, 4, and 8 m.

Salinas et al. (2022) [13] proposed an easy-to-implement correction function to be used in conjunction with the well-mixed model to account for the departure from well-mixedness. Here again, RANS2 showed quantitative differences compared to LES, however it was able to capture the correct trends of the time-dependent correction function and its asymptotic steady-state value. For example, for a separation distance of 2 m, the correction function from RANS2 was around  $\gamma_{\infty}=1.8$ , whereas for LES, it was around  $\gamma_{\infty}=1.5$ .

In the case of LES, the number of CPU hours necessary to reach a statistically stationary state and then to gather statistics is approximately 260,000 CPU hours. An equivalent RANS simulation requires approximately 45,000 CPU hours. Overall, the present results indicate that RANS2  $k-\varepsilon$  realizable may be used as a computationally cheaper alternative to LES as a tool for predicting pathogen concentration in confined spaces albeit, with potentially increased statistical discrepancy. Nonetheless, the present study only considered a limited configuration with a single geometry of a canonical room as well as a single shape and placement of the ventilation system. Future RANS and LES studies should explore different geometries and ventilation configurations and compare results. Only then, can a more definitive conclusion be drawn as to the suitability of RANS for the problem at hand.

Finally, we should note that practical scenarios will include heating/cooling, which will alter the flow through natural convection. A satisfactory investigation of the effects of temperature, would require exploring parameters such as the intensity of the heat source, distribution, number, size and location of sources, etc. However, our purpose here is to assess the efficacy of RANS simulations in predicting the droplet nuclei distribution within the room, which could be assessed by comparison against LES in the absence of heating/cooling. Furthermore, from a practical point of view, and since the data was shown to collapse for different values of ACH, the results of this study may be used in the case of high ACH, where the effect of natural convection is small.

# CRediT authorship contribution statement

K. Choudhary: Methodology, Software, Conceptualization, Validation, Investigation, Writing – review & editing, Visualization. K.A. Krishnaprasad: Methodology, Software, Validation, Investigation, Conceptualization. S. Pandey: Methodology, Software, Validation, Visualization, Conceptualization. N. Zgheib: Conceptualization, Writing – original draft, Writing – review & editing, Supervision. J.S. Salinas: Conceptualization. M.Y. Ha: Conceptualization, Methodology, Resources, Writing – review & editing, Supervision, Project administration, Funding acquisition. S. Balachandar: Conceptualization, Methodology, Resources, Writing – review & editing, Supervision, Project administration, Funding acquisition.

#### Data availability

Data will be made available on request.

### Acknowledgments

We gratefully acknowledge support from NSF, USA (EAGER Grant no. 2134083), LG Electronics, Korea (Grant no. C2021017165) and University of Florida Informatics Institute, USA.

#### References

- Dbouk T, Drikakis D. On coughing and airborne droplet transmission to humans. Phys Fluids 2020;32(5):053310.
- [2] Liu K, Allahyari M, Salinas J, Zgheib N, Balachandar S. Investigation of theoretical scaling laws using large eddy simulations for airborne spreading of viral contagion from sneezing and coughing. Phys Fluids 2021;33(6):063318.
- [3] Li M, Chong KL, Ng CS, Bahl P, de Silva CM, Verzicco R, Doolan C, MacIntyre CR, Lohse D. Towards realistic simulations of human cough: Effect of droplet emission duration and spread angle. Int J Multiph Flow 2022;147:103883.
- [4] Fabregat A, Gisbert F, Vernet A, Ferré JA, Mittal K, Dutta S, Pallarès J. Direct numerical simulation of turbulent dispersion of evaporative aerosol clouds produced by an intense expiratory event. Phys Fluids 2021;33(3):033329.
- [5] Dbouk T, Drikakis D. On airborne virus transmission in elevators and confined spaces. Phys Fluids 2021;33(1):011905.
- [6] Zhang Z, Capecelatro J, Maki K. On the utility of a well-mixed model for predicting disease transmission on an urban bus. AIP Adv 2021;11(8):085229.
- [7] Foster A, Kinzel M. Estimating COVID-19 exposure in a classroom setting: A comparison between mathematical and numerical models. Phys Fluids 2021;33(2):021904.
- [8] Mathai V, Das A, Breuer K. Aerosol transmission in passenger car cabins: Effects of ventilation configuration and driving speed. Phys Fluids 2022;34(2):021904.
- [9] Schimmoller BJ, Trovão NS, Isbell M, Goel C, Heck BF, Archer TC, Cardinal KD, Naik NB, Dutta S, Daniel AR, et al. Covid-19 exposure assessment tool (CEAT): Easy-to-use tool to quantify exposure based on airflow, group behavior, and infection prevalence in the community. 2022, MedRxiv.
- [10] Liu K, Allahyari M, Salinas JS, Zgheib N, Balachandar S. Peering inside a cough or sneeze to explain enhanced airborne transmission under dry weather. Sci Rep 2021;11(1):1–9.
- [11] Stiehl B, Shrestha R, Schroeder S, Delgado J, Bazzi A, Reyes J, Kinzel M, Ahmed K. The effect of relative air humidity on the evaporation timescales of a human sneeze. AIP Adv 2022;12(7):075210.
- [12] Bazant MZ, Bush JW. A guideline to limit indoor airborne transmission of COVID-19. Proc Natl Acad Sci 2021;118(17).
- [13] Salinas JS, Krishnaprasad K, Zgheib N, Balachandar S. Improved guidelines of indoor airborne transmission taking into account departure from the well-mixed assumption. Phys Rev Fluids 2022:7(6):064309.
- [14] Wells W, Contagion A, Hygiene A. An ecological study of droplet infections. Cambridge University Press; 1955.
- [15] Riley E, Murphy G, Riley R. Airborne spread of measles in a suburban elementary school. Am J Epidemiol 1978;107(5):421–32.
- [16] Dbouk T, Drikakis D. On respiratory droplets and face masks. Phys Fluids 2020;32(6):063303.
- [17] Yi H, Wang Q, Feng Y. Computational analysis of obstructive disease and cough intensity effects on the mucus transport and clearance in an idealized upper airway model using the volume of fluid method. Phys Fluids 2021;33(2):021903.
- [18] Zhao J, Feng Y, Koshiyama K, Wu H. Prediction of airway deformation effect on pulmonary air-particle dynamics: A numerical study. Phys Fluids 2021;33(10):101906.
- [19] Zhang Y, Feng G, Kang Z, Bi Y, Cai Y. Numerical simulation of coughed droplets in conference room. Procedia Eng 2017;205:302–8.
- [20] Feng Y, Marchal T, Sperry T, Yi H. Influence of wind and relative humidity on the social distancing effectiveness to prevent COVID-19 airborne transmission: A numerical study. J Aerosol Sci 2020;147:105585.
- [21] Jahanbin A, Semprini G. Integrated effects of the heat recovery ventilation and heat source on decay rate of indoor airborne particles: A comparative study. J Build Eng 2022;50:104156.
- [22] Zeng G, Chen L, Yuan H, Yamamoto A, Chen H, Maruyama S. Analysis of airborne sputum droplets flow dynamic behaviors under different ambient conditions and aerosol size effects. Chemosphere 2022;307:135708.

- [23] Bahramian A, Mohammadi M, Ahmadi G. Effect of indoor temperature on the velocity fields and airborne transmission of sneeze droplets: An experimental study and transient CFD modeling. Sci Total Environ 2023;858:159444.
- [24] Jahanbin A, Semprini G. Combined impacts of the ceiling radiant cooling and ventilation on dispersion and deposition of indoor airborne particles. Therm Sci Eng Prog 2022;34:101438.
- [25] ANSYS. ANSYS fluent theory guide 2019 R2. 2019.
- [26] Choi H, Oh J, Park M, Oh S, Park Y, Ha M. Investigation of the cooling performance and thermal comfort for 4-way cassette air conditioner with swinging motion of vanes. J Mech Sci Technol 2021;35.
- [27] Liu W, Lian Z, Yao Y. Optimization on indoor air diffusion of floor-standing type room air-conditioners. Energy Build 2008;40:59–70.
- [28] Yongson O, Badruddin IA, Zainal Z, Aswatha Narayana P. Airflow analysis in an air conditioning room. Build Environ 2007;42(3):1531–7.
- [29] Luo K, Yu H, Dai Z, Fang M, Fan J. CFD simulations of flow and dust dispersion in a realistic urban area. Eng Appl Comput Fluid Mech 2016;10(1):228–42.
- [30] Teodosiu C, Hohota R, n GRA, Woloszyn M. Numerical prediction of indoor air humidity and its effect on indoor environment. Build Environ 2003;38(5):655–64.
- [31] Mofakham AA, Ahmadi G. Particles dispersion and deposition in inhomogeneous turbulent flows using continuous random walk models. Phys Fluids 2019;31(8):083301.
- [32] Dehbi A. Turbulent particle dispersion in arbitrary wall-bounded geometries: A coupled CFD-Langevin-equation based approach. Int J Multiph Flow 2008;34(9):819–28.
- [33] Bocksell TL, Loth E. Stochastic modeling of particle diffusion in a turbulent boundary layer. Int J Multiph Flow 2006;32:1234–53.
- [34] Mito Y, Hanratty TJ. Use of a modified langevin equation to describe turbulent dispersion of fluid particles in a channel flow. Flow Turbul Combust 2002;68. http://dx.doi.org/10.1023/A:1015614823809, URL https://link. springer.com/article/10.1023/A:1015614823809#citeas.
- [35] Mofakham AA, Ahmadi G. On random walk models for simulation of particle-laden turbulent flows. Int J Multiph Flow 2020;122:103157.
- [36] Ferry J, Balachandar S. A fast Eulerian method for disperse two-phase flow. Int J Multiph Flow 2001;27:1199–226. http://dx.doi.org/10.1016/S0301-9322(00) 00069-0.
- [37] Ferry J, Balachandar S. Equilibrium expansion for the Eulerian velocity of small particles. Powder Technol 2002;125(2):131–9. http://dx.doi.org/10.1016/S0032-5910(01)00499-5.
- [38] Balachandar S, Liu K, Lakhote M. Self-induced velocity correction for improved drag estimation in Euler-Lagrange point-particle simulations. J Comput Phys 2019;376:160–85.
- [39] Pozorski J, Minier J-P. On the Lagrangian turbulent dispersion models based on the Langevin equation. Int J Multiph Flow 1998;24(6):913–45. http://dx.doi.org/ 10.1016/S0301-9322(98)00016-0, URL https://www.sciencedirect.com/science/ article/pii/S0301932298000160.
- [40] Fede P, Simonin O, Villedieu P, Squires K. Stochastic modeling of the turbulent subgrid fluid velocity along inertial particle trajectories. In: Proceedings of the summer program. Center for Turbulence Research; 2006, p. 247–58.
- [41] Liu K, Huck P, Aliseda A, Balachandar S. Investigation of turbulent inflow specification in Euler-Lagrange simulations of mid-field spray. Phys Fluids 2021;33(3):033313.
- [42] Haworth DC, Pope SB. A generalized langevin model for turbulent flows. Phys Fluids 1986;29(2):387–405. http://dx.doi.org/10.1063/1.865723.
- [43] Yoshizawa A. A statistically-derived subgrid model for the large-eddy simulation of turbulence. Phys Fluids 1982;25(9):1532–8. http://dx.doi.org/10.1063/ 1.863940.
- [44] Quinn W. On mixing in an elliptic turbulent free jet. Phys Fluids A Fluid Dyn 1989;1(10):1716–22.
- [45] Gutmark E, Grinstein F. Flow control with noncircular jets. Annu Rev Fluid Mech 1999;31(1):239–72.
- [46] Liu K, Zgheib N, Balachandar S. On the spreading of non-canonical thermals from direct numerical simulations. Phys Fluids 2020;32(2):026602.
- [47] Zgheib N, Bonometti T, Balachandar S. Long-lasting effect of initial configuration in gravitational spreading of material fronts. Theor Comput Fluid Dyn 2014;28(5):521–9.
- [48] Zgheib N, Bonometti T, Balachandar S. Dynamics of non-circular finite-release gravity currents. J Fluid Mech 2015;783:344–78.
- [49] Zhu S, Zgheib N, Balachandar S, Ooi A. Front dynamics of elliptical gravity currents on a uniform slope. Phys Rev Fluids 2017;2(6):064801.